AIP | The Journal of Chemical Physics

Scattering intensity of bicontinuous microemulsions and sponge phases

Matti Peltomäki, Gerhard Gompper, and Daniel M. Kroll

Citation: J. Chem. Phys. **136**, 134708 (2012); doi: 10.1063/1.3701265
View online: http://dx.doi.org/10.1063/1.3701265
View Table of Contents: http://jcp.aip.org/resource/1/JCPSA6/v136/i13
Published by the American Institute of Physics.

Scattering intensity of bicontinuous microemulsions and sponge phases

Matti Peltomäki,[1] Gerhard Gompper,[1] and Daniel M. Kroll[2]
[1]*Theoretical Soft Matter and Biophysics, Institute of Complex Systems, Forschungszentrum Jülich, Jülich 52425, Germany*
[2]*Department of Physics, NDSU Department 2755, North Dakota State University, Fargo, North Dakota 58108-6050, USA*

(Received 13 February 2012; accepted 20 March 2012; published online 6 April 2012)

Monte Carlo simulations of dynamically triangulated surfaces of variable topology are used to investigate the scattering intensities of bicontinuous microemulsions. The bulk scattering intensity is shown to follow the Teubner-Strey expression. The domain size and the correlation length are extracted from the scattering peaks as a function of the bending rigidity, saddle-splay modulus, and surfactant density. The results are compared to earlier theories based on Ginzburg-Landau and Gaussian random field models. The ratio of the two length scales is shown to be well described by a linear combination of logarithmically renormalized bending rigidity and saddle-splay modulus with universal prefactors. This is in contrast to earlier theoretical predictions in which the scattering intensity is independent of the saddle-splay modulus. The equation of state, and the asymptotics of the bulk and film scattering intensities for high and low wave vectors are determined from simulations and compared with theoretical results. © *2012 American Institute of Physics*. [http://dx.doi.org/10.1063/1.3701265]

I. INTRODUCTION

Mixtures of water, oil, and surfactant encompass a large variety of mesoscopic structures, including lamellar, hexagonal, cubic, and micellar phases. For low surfactant densities, a particularly interesting and important phase is the macroscopically homogeneous and isotropic microemulsion phase.[1,2] In all these phases, it is energetically favorable for the surfactant to form monolayers at the microscopic oil-water interface, with the hydrophilic head on the water side and the hydrophobic tail on the oil side; this induces the formation of water-rich and oil-rich domains. For microemulsions, an extensive monolayer separates space into two intertwined volumes, rich in water and oil, respectively, both of which are continuous. Due to this property, such phases are called bicontinuous. The surfactant monolayers have typically a vanishing interface tension.[3,4] Consequently, the properties of the mixture are largely governed by the bending rigidity of surfactant monolayers.[5–9]

A closely related system is found in binary mixtures of water and surfactant, also for low surfactant densities, in which the surfactant tends to form bilayers with the hydrophilic ends exposed. In a narrow region of phase space, this leads to the separation of the solvent into two continuous domains by the surfactant bilayer. Such configurations are called L_3 phases or sponge phases.[10] The L_3 phase often coexists with a lamellar phase or a highly dilute surfactant solution, or both. In addition to the general structure, sponge phases share many properties with symmetric oil-water microemulsions, including vanishing interface tension and spontaneous curvature.

Small-angle neutron scattering is among the most important experimental techniques to investigate and characterize the structure and dynamics of microemulsions and sponge phases,[11–13] to elucidate the role of additives such as amphiphilic block copolymers[14–17] or non-absorbing polymers,[18,19] and to understand the behavior of unconventional microemulsions containing supercritical CO_2 instead of oil.[20,21] As microemulsions with new components and additives become important for future applications, it is important to understand in more detail which information about the emergent properties of the surfactant membranes can be extracted from a scattering experiment.

Depending on the sample preparation, the scattering can take place either in bulk contrast or in film contrast. In the former, the neutrons scatter from one of the solvents, and the scattering reveals the structure of the bulk phases. In the latter, the neutrons scatter from either the surfactant or additive substances in the surfactant layer, and the scattering probes the structure of the interface. Only the latter technique is available for sponge phases. The scattering experiments typically lead to a peak with a finite width in the bulk scattering, and a weaker peak or a shoulder in the film scattering. Other experimental scattering methods include neutron spin echo,[22,23] dynamic light scattering,[24] and small-angle x-ray scattering.[25,26] The phase diagrams of solvent-surfactant systems have been predicted theoretically by employing coarse-grained lattice models of fluctuating membranes,[27–31] as well as lattice models of three-component amphiphilic mixtures.[32]

Since the structure of microemulsions is dominated by the curvature elasticity of the surfactant layer, a crucial step in understanding it is to identify how the scattering peaks follow from the elastic properties of the surfactant membrane. The first theories[11,33,34] were phenomenological theories of the Ginzburg-Landau type. In them, Gaussian fluctuations of the order-parameter field determine the scattering intensity, which is given by the so-called Teubner-Strey formula for bulk scattering. It gives the correct functional form of the scattering intensity at and in the vicinity of the peak. Because of the phenomenological form of the theory, the

parameters of the formula cannot be connected easily with material properties.

A later approach, which attempted to improve on the phenomenological theory, is the Gaussian random field model (GRFM).[35,36] In it, the structure of the surfactant monolayer is described by the level set of a Gaussian random scalar field for which a two-point interaction kernel is chosen so that the free-energy density in GRFM is as close as possible to the free-energy density given by a curvature Hamiltonian. The GRFM gives the same expression for the bulk scattering intensity as the phenomenological theory but also predicts all parameters as a function of the material properties. The most important prediction is that all features of the scattering peak – its amplitude, position, and width – depend only on the bending rigidity, the temperature, and the surfactant density but are *independent of the saddle-splay modulus*. The predictions of the GRFM have been used to analyze scattering experiments in Refs. 15, 16, and 20. These analyses show that it is necessary to augment the GRFM results by the logarithmic renormalization[37] of the bending rigidity, which arises from thermal fluctuations on length scales smaller than the characteristic domain size.[15,16,38–42]

The aim of our study is to determine the structure of microemulsions and sponge phases by Monte Carlo (MC) simulations of dynamically triangulated surfaces with fluctuating topology, following Ref. 43. The advantage of this approach is that an ensemble of thermally fluctuating membranes — with shapes and topologies controlled by bending rigidity and saddle-splay modulus — and the resulting scattering intensities can be calculated without resorting to any approximations. Our language, when referring to the model system is that of microemulsions; however, at the level of abstraction we employ, the discussion is equally valid for both a balanced ternary microemulsion with a surfactant monolayer, or a sponge phase with a surfactant bilayer. We calculate the bulk and film scattering intensity of the simulated configurations, and concentrate especially on the dimensionless ratio of domain size and correlation length, which is extracted from the scattering intensity in bulk contrast. This allows, for the first time, a stringent test of the accuracy of previous theoretical predictions. As the main result, we demonstrate that in contrast to the existing theoretical predictions, the length scale ratio strongly depends on the saddle-splay modulus. We also study the high-q tail of the scattering intensities, the equation of state of the microemulsion, and long-wavelength properties of the film scattering intensity. The behavior of these quantities are compared to the predictions of earlier work and provide useful consistency checks and additional detailed information about the microemulsion phase.

This paper is organized as follows. In Sec. II, we briefly summarize the theoretical background of microemulsion scattering. In Sec. III, the Monte Carlo simulations of dynamically triangulated surfaces with fluctuating topology are explained in detail, together with the procedure to compute the scattering intensities from the simulated configurations. In Sec. IV, we present our results concerning the equation of state, bulk and film scattering intensities, and the topology of the sponge phase. Finally, the results are discussed and the paper is concluded in Sec. V.

II. THEORETICAL BACKGROUND

A. Ginzburg-Landau theory

The first attempt to explain the structure of microemulsions theoretically is given by the phenomenological Ginzburg-Landau theory for microemulsions.[11] The model is defined by the free-energy functional[38,44]

$$\mathcal{F}[\psi] = \frac{1}{a}\int [f(\psi) + g(\psi)(\nabla\psi)^2 + (\Delta\psi)^2]\mathrm{d}^3r, \tag{1}$$

where $\psi(\vec{r})$ is a three-dimensional scalar order-parameter field, which is identified with the local density difference between the two bulk solvents. The amphiphile concentration does not appear explicitly, and should be considered integrated out. The functions $f(\psi)$ and $g(\psi)$ are chosen as[45]

$$f(\psi) = \omega(\psi - \psi_o)^2(\psi^2 + f_0)(\psi - \psi_w)^2, \tag{2}$$

$$g(\psi) = b + g_2\psi^2. \tag{3}$$

Here, $a > 0$ and $\omega > 0$ are necessary to obtain thermodynamically stable systems. The choice of Eq. (2) corresponds to a three-phase coexistence of an oil-rich phase at $\psi = \psi_0$, a water-rich phase at $\psi = \psi_w$, and a microemulsion at $\psi = 0$. In order to concentrate on the microemulsion phase, Eqs. (2) and (3) are further simplified assuming small ψ. This leads to $f(\psi) = c\psi^2$ and $g(\psi) = b$, where constant contributions to $f(\psi)$ are ignored, and the linear ψ-term in f vanishes for symmetric microemulsions with $\psi_o = -\psi_w$. Altogether, these simplifications lead to

$$\mathcal{F}[\psi] = \frac{1}{a}\int [c\psi^2 + b(\nabla\psi)^2 + (\Delta\psi)^2]\mathrm{d}^3r. \tag{4}$$

A negative value of the coefficient b makes the amphiphilic monolayers energetically preferable. The bulk scattering intensity resulting from Eq. (4) is[11]

$$S_b(q) = \frac{a}{q^4 + bq^2 + c}. \tag{5}$$

This equation, with $b < 0$, was demonstrated to match experiments rather well in Ref. 11, as well as in several later experimental studies, see, e.g., Refs. 12, 15, 16, and 20. Note that this phenomenological theory needs further input from a more microscopic model to predict the coefficients a, b, and c as a function of microscopic parameters of the system.

The correlation function corresponding to Eq. (5) is

$$g_b(r) = \frac{\sin(k_0 r)}{k_0 r}\exp\left(-\frac{r}{\xi}\right). \tag{6}$$

As a characteristic feature of microemulsions, Eq. (6) contains two length scales, the domain size of the structure, $d = 2\pi/k_0$, and the decay length, ξ, associated with the absence of long-range order. In terms of the parameters of the scattering intensity (Eq. (5)), these length scales are given by[11]

$$k_0 = \frac{1}{2}\sqrt{2\sqrt{c} + b}\ ;\ \xi^{-1} = \frac{1}{2}\sqrt{2\sqrt{c} - b}. \tag{7}$$

B. Gaussian random field model and membrane curvature elasticity

The GRFM, in combination with the membrane curvature Hamiltonian, makes additional predictions for the scattering intensity as a function of the properties of the amphiphilic monolayer.[35,36] Like in Ginzburg-Landau theory, the starting point is a three-dimensional scalar order-parameter field $\psi(\vec{r})$. In Fourier space, the order-parameter fluctuations are governed by the Hamiltonian[35]

$$H_t = \frac{1}{2}\sum_{\vec{q}} V(\vec{q})\psi(\vec{q})\psi(-\vec{q}), \tag{8}$$

where the sum is over all possible wave vectors $\vec{q}$ and $V(\vec{q})$ is a so far arbitrary potential of a two-body interaction. In addition, the constraint $\langle\psi(\vec{r})\rangle_{\vec{r}} = 1$ is applied.

In order to fix $V(\vec{q})$ and consequently make further analysis possible, the amphiphilic monolayer is considered as a mathematical surface, with its shape and fluctuations controlled by the curvature energy[46]

$$\frac{\mathcal{H}}{k_B T} = \int_S \mathrm{d}S[2\kappa(H - c_0)^2 + \bar{\kappa}K], \tag{9}$$

where $H = (H_1 + H_2)/2$ is the mean curvature and $K = H_1H_2$ the Gaussian curvature, both expressed in terms of the local principal curvatures H_1 and H_2, and the integral is over the whole surface S. The material properties of the membrane are contained in three elastic parameters, the dimensionless bending rigidity κ, the saddle-splay modulus $\bar{\kappa}$, and the spontaneous curvature c_0. We consider here only sponge phases and balanced microemulsions with $c_0 = 0$.

In the GRFM, the interaction kernel $V(\vec{q})$ is chosen such that the difference in the free-energy density between the two Hamiltonians of Eqs. (8) and (9) is minimized.[35] This results in a $V(\vec{q})$ whose inverse is the bulk scattering intensity given in Eq. (5). However, the parameters, most importantly b and c, can now be expressed in terms of the bending rigidity κ and the area density of the surface. For large κ, the parameters are[15,35]

$$b = \frac{3}{2}\pi^2\left(\frac{S}{V}\right)^2, \tag{10}$$

$$c = \left(\frac{3}{4}\pi^2\right)^2\left(\frac{S}{V}\right)^4. \tag{11}$$

This determines the (inverse) length scales k_0 and ξ^{-1} via Eq. (7). Additionally, the inverse of the area density S/V, where S is the total membrane area in the system, and V the system volume, is a natural structural length scale, in units of which the other lengths are conveniently measured. Finally, the predictions for the length scales and their dimensionless ratio $k_0\xi$ become[15]

$$k_0 = \frac{\sqrt{3}}{2}\pi\frac{S}{V}, \tag{12}$$

$$\xi = \frac{128}{15\pi}\left(\frac{S}{V}\right)^{-1}\kappa, \tag{13}$$

$$k_0\xi = \frac{64}{5\sqrt{3}}\kappa. \tag{14}$$

In both Eqs. (13) and (14), the temperature does not appear since κ is dimensionless, as defined in Eq. (9). According to GRFM, the characteristic wave vector k_0 is independent of the elastic properties of the membrane and the correlation length ξ is proportional to κ. The most remarkable feature of Eqs. (12)–(14) is, however, the complete lack of dependence on the saddle-splay modulus $\bar{\kappa}$.

C. Bending rigidity renormalization

For membranes and surfaces with vanishing surface tension, the bending rigidity κ and the saddle-play modulus $\bar{\kappa}$ on a length scale l are renormalized by thermal fluctuations on smaller scales.[37] More precisely, the elastic membrane parameters are predicted to vary as[37,47–49]

$$\kappa_R(l) = \kappa - \alpha\frac{1}{4\pi}\ln(l/\delta), \tag{15}$$

$$\bar{\kappa}_R(l) = \bar{\kappa} - \bar{\alpha}\frac{1}{4\pi}\ln(l/\delta), \tag{16}$$

where δ is an effective cutoff of the fluctuation wavelengths of the membrane and $l = V/S$ is the structural length scale given by the surfactant density. The coefficients α and $\bar{\alpha}$ are universal prefactors. Their values have been under debate, but most calculations[37,48] arrive at the values $\alpha = 3$ and $\bar{\alpha} = -10/3$. There is also numerical and experimental evidence in favor of these values.[16,41,43] In the remainder of this contribution, we use them in our numerical analysis. We employ the minimum distance a_0 between two vertices as the cutoff δ.

The renormalization of $\bar{\kappa}$ is essential to understand the transition between the lamellar and bicontinuous phases of surfactant solutions. The renormalized saddle-splay modulus $\bar{\kappa}_R$ is negative for small l (note that the bare value $\bar{\kappa} < 0$), increases with increasing length scale — corresponding to decreasing surfactant density — and finally vanishes. This happens at the boundary between the lamellar and bicontinuous phases, where $\bar{\kappa}_R = 0$.[29,30]

D. Film scattering

So far, all theoretical expressions we have discussed have been for bulk scattering. While similar treatment for the scattering in film contrast is more complicated, certain issues can still be addressed. The Ginzburg-Landau model of Sec. II A has been extended to include the surfactant density, and the film scattering intensity has been calculated in a perturbative expansion in the coupling between the two order parameters.[50,51] In GRFM, the film correlation function for large r is well approximated by[36]

$$g_{ff}^{(\infty)}(r) = \left(\frac{S}{V}\right)^2 + \frac{2}{\pi^2}\left[\tau g_b(r)^2 - \frac{2}{3}g_b'(r)^2 + \frac{1}{9\tau}g_b''(r)^2\right], \tag{17}$$

where $g_b'(r)$ and $g_b''(r)$ are the first and second derivatives of $g_b(r)$ with respect to r, and

$$\tau = \left(\frac{\pi}{2}\right)^2\left(\frac{S}{V}\right)^2. \tag{18}$$

Equation (17) implies, in particular, that whenever there is a peak in the bulk scattering intensity at k_0 for a given system, the film scattering intensity has a peak or at least a shoulder at $2k_0$.

The film scattering intensity in the GRFM approach has then been calculated in two ways. First, in Ref. 36 scattering intensity was computed numerically by using the exact GRFM expression for the film correlation function. Second, in Ref. 15 the film scattering intensity was calculated analytically by using the approximate expression of Eq. (17); it has then been combined with a film scattering intensity according to the Porod law, Eq. (21), corresponding to a film scattering function $g_{ff}^{(0)}(r) \propto r^{-1}$ for small r. The combined expression was then shown to reproduce experimental data after a fitting procedure.[15]

Both theoretical approaches, Ginzburg-Landau and GRFM, agree in their prediction that the film scattering intensity for small q has the form[36,50,51]

$$S_f(q) = \alpha + \beta \frac{1}{q} \arctan\left(\frac{\xi q}{2}\right). \tag{19}$$

Here, α and β are constants. Since $\arctan(\frac{\xi q}{2})$ tends to a constant for large $q\xi$, this is equivalent to $1/q$-behavior for $1 < q\xi < k_0\xi$. Furthermore, in both theoretical approaches a peak, a shoulder, or a monotonous decay of the film scattering intensity is found for large, intermediate, and small $k_0\xi$, respectively.[36,51]

E. Porod laws

The scattering intensities in both bulk and film contrast for large $\vec{q}$ are dominated by the local interface profile. In bulk scattering, the Porod law[12,52] states that

$$S_b(q) = 2\pi(\Delta\rho)^2 \frac{S}{V} q^{-4} \exp(-q^2\Sigma^2), \tag{20}$$

where $\Delta\rho$ is the scattering length difference between the two bulk phases, and Σ is the roughness of the interface. The q^{-4} decay of the intensity for high q is the same power law as predicted both by the phenomenological theory and the GRFM, Eq. (5). However, the Porod law has a different origin, since it only probes the surfaces at short length scales and does not see the correlations between different surfaces. This is manifested by the fact that the predicted amplitude is different. This gives a convenient way to distinguish between the intermediate-q regime corresponding to alternating oil and water phases, and the high-q Porod regime.

Similarly, the Porod law for film scattering reads[53]

$$S_f(q) = 2\pi(\Delta\rho)^2 t^2 \frac{S}{V} q^{-2} \exp\left(-q^2 t_{\text{eff}}^2\right), \tag{21}$$

where t is the film thickness and $t_{\text{eff}} = \sqrt{t^2/12 + \Sigma^2}$, where Σ is the surface roughness.[15]

III. SIMULATIONS

A. Monte Carlo of dynamically triangulated surfaces

We employ MC simulations of dynamically triangulated surfaces,[7,54] which we amend for fluctuating topology following Refs. 42 and 43.

In the simulations, the membrane is modeled as a triangulated surface, with beads of diameter a_0 at the vertices. Denote the number of beads in the surface by N, the number of bonds by N_b, and the number of triangles by N_t. The beads are not allowed to overlap. To this end, the potential

$$V_{HS}(r) = \begin{cases} \infty & \text{if } r < a_0 \\ 0 & \text{otherwise} \end{cases} \tag{22}$$

between *all* pairs of vertices is applied. Here, r is the distance between the vertices. The edges of the triangulation play the role of tethers connecting the beads and they are modeled as having a maximum finite extension but otherwise no contribution to the energy. In other words, the potential

$$V_{ME}(r) = \begin{cases} 0 & \text{if } r < \ell_0 \\ \infty & \text{otherwise} \end{cases} \tag{23}$$

is applied for all pairs of vertices *connected by an edge*. If the parameters above are chosen such that $\ell_0/a_0 < \sqrt{3}$, the membrane is self-avoiding.[7] Here, we use $\ell_0/a_0 = \sqrt{8/3} \approx 1.633$.

The energy corresponding to the first term of Eq. (9) can only be applied through an explicit discretization. Here, we use the discretization[41,55,56]

$$V_{BR} = \frac{\kappa}{2} \sum_{i=1}^{N} \frac{1}{\sigma_i} \left\{ \sum_{j \in N_i} \frac{\sigma_{i,j} \vec{r}_{i,j}}{r_{i,j}} \right\}^2, \tag{24}$$

where N_i is the set of neighbors of vertex i, $\vec{r}_{i,j}$ is the bond vector from vertex i to vertex j, and $r_{i,j} = |\vec{r}_{i,j}|$ its length, $\sigma_{i,j} = r_{i,j}[\cot(\theta_1) + \cot(\theta_2)]$ is the length of the bond between vertices i and j in the dual lattice with θ_1 and θ_2 being the angles opposite to the bond in the two triangles neighboring it, and finally

$$\sigma_i = \frac{1}{4} \sum_{j \in N_i} \sigma_{i,j} r_{i,j} \tag{25}$$

is the area of the dual cell of vertex i.

The last term of Eq. (9), in turn, can be treated by using the Gauss-Bonnet theorem

$$\frac{1}{2\pi} \int_S \mathrm{d}S K = \chi_E = N - N_b - N_t, \tag{26}$$

where the topological invariant χ_E is called the Euler characteristic of the closed surface S.

Using the sum of the three potentials in Eqs. (22)–(24), a MC simulation of the membrane can be constructed as follows. A MC step consists of N attempts to move a randomly chosen particle by a displacement chosen uniformly at random in the cube $[-s, s]^3$. A move is accepted with probability equal to $\min(1, \exp(\Delta E))$,[57] where $\Delta E = E_{\text{old}} - E_{\text{new}}$ is the difference in the total energy between the configurations

before and after the attempt. We choose s so that approximately 50% of the moves are accepted. The temperature does not appear explicitly in these expressions since $\beta^{-1} = k_B T$ has been absorbed in the units of energy. Note that were there no bending energy, all moves which do not violate the constraints of maximum tether extension and non-overlap of the beads would be accepted.

The simulation model as described up to now does not allow movement, diffusive or otherwise, of the beads within the surface. Such is, however, necessary, since the surfactant monolayers modeled here are fluid. To overcome this, bond flips are introduced. We consider two neighboring triangles, i.e., systems of four beads. They necessarily have exactly one diagonal connection out of two possible ones. An attempted bond flip is then an attempt to remove the diagonal tether and replace it with another possibility. As above, the energy of the surface is evaluated before and after the attempt, which is then accepted with probability $\min(1, \exp(\Delta E))$ in order to satisfy detailed balance.

Note that due to the Gauss-Bonnet theorem, Eq. (26), the second term on the right-hand side of Eq. (9) is topological invariant and does not affect the Monte Carlo steps described above.

In the simulations, we use a constant pressure ensemble. The primary motivation is to avoid problems with two-phase coexistence regions, but this choice also has the additional advantage that one gains direct access to the equation of state, since the surfactant density ϕ can be determined as a function of the applied external pressure.

B. Fluctuating topology

So far, the topology of the surface has been fixed. However, bicontinuous microemulsions show a rich microscopic structure, where the topology of the surfactant monolayer fluctuates in an equilibrium state, and varies after a quench from one state to another. Therefore, including topology changes in the MC simulation scheme described above is essential. Here, we follow Refs. 42 and 43 and use the topology change shown schematically in Fig. 1. It consists of either inserting or cutting minimal necks between two distinct membrane segments.

We now describe this step in detail. Let the variable s characterize the state of the system. The probability of state s is $P(s) \sim \exp[-\mathcal{H}(s)]$, where $\mathcal{H}$ is the curvature energy in units of $k_B T$ of the system in state s, given by Eq. (9), where now, in contrast to the vertex-displacement and bond-flip steps described above, the Gaussian-curvature term plays an essential role. Two states s and s' are linked by a transition probability $w(s \to s')$ of going from state s to s'. The condition of "microscopic reversibility" or detailed balance,

$$P(s)w(s \to s') = P(s')w(s' \to s), \tag{27}$$

is then sufficient to guarantee that the systems reaches the equilibrium state characterized by the Gibbs ensemble.

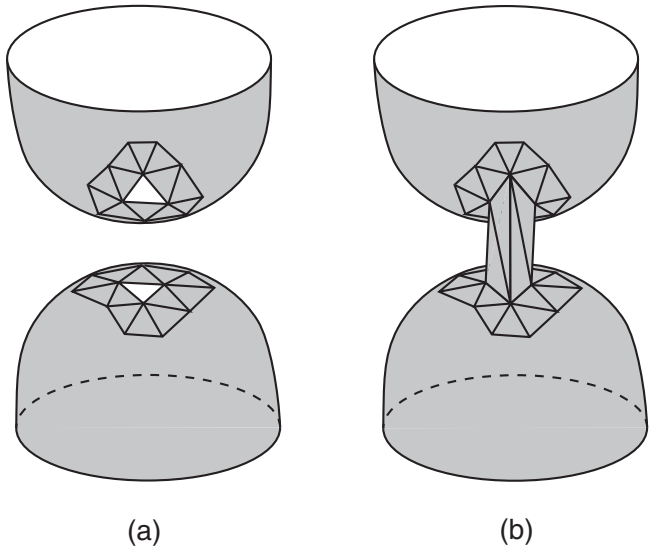

FIG. 1. Monte Carlo step for changing the topology of a triangulated surface. (a) Two surface triangles are removed. (b) The two holes are connected by a prism of six triangles.

The transition probabilities are[43]

$$w(s \to s') = \begin{cases} a_{ss'} & \text{for} \quad a_{s's} P(s') \geq a_{ss'} P(s) \\ a_{ss'} \frac{a_{s's} P(s')}{a_{ss'} P(s)} & \text{for} \quad a_{s's} P(s') < a_{ss'} P(s) \end{cases}. \tag{28}$$

The stochastic matrix element $a_{ss'}$ for making a neck starting in state s is $a_{ss'} = 2p/N_t(s)$; for destroying a neck when in state s', it is $a_{s's} = 6(1-p)/N_t(s')$. Here, p is the probability that we try to create a neck for a chosen surface triangle, and $(1-p)$ is the probability that we try to destroy a neck. In the first case, the factor 2 arises since when trying to create a neck, there are two surface triangles that would lead to the same result; in the second, the factor is 6 since there are six surface triangles in a neck, and the choice of any of the six will lead to the destruction of the neck with equal probability. The choice (Eq. (28)) guarantees that Eq. (27) is fulfilled. The move from s to s' should be accepted with probability[57]

$$\min\left(1, \frac{a_{s's} P(s')}{a_{ss'} P(s)}\right). \tag{29}$$

In this algorithm, a surface triangle is chosen at random, and an attempt is made to generate a neck three times as often as an attempt to destroy a neck. This means that $p = 3/4$. When attempting to create a neck in the move $s \to s'$, the move is accepted with the probability

$$\min\left(1, \frac{N_t(s)}{N_t(s')} \exp[\mathcal{H}(s) - \mathcal{H}(s')]\right), \tag{30}$$

where $N_t(s') = N_t(s) + 4$. Similarly, when attempting to destroy a neck, the move is accepted with the probability

$$\min\left(1, \frac{N_t(s)}{N_t(s')} \exp[\mathcal{H}(s) - \mathcal{H}(s')]\right), \tag{31}$$

where $N_t(s') = N_t(s) - 4$.

In a simulation with a fixed number of vertices and variable topology, the number of triangles and bonds must

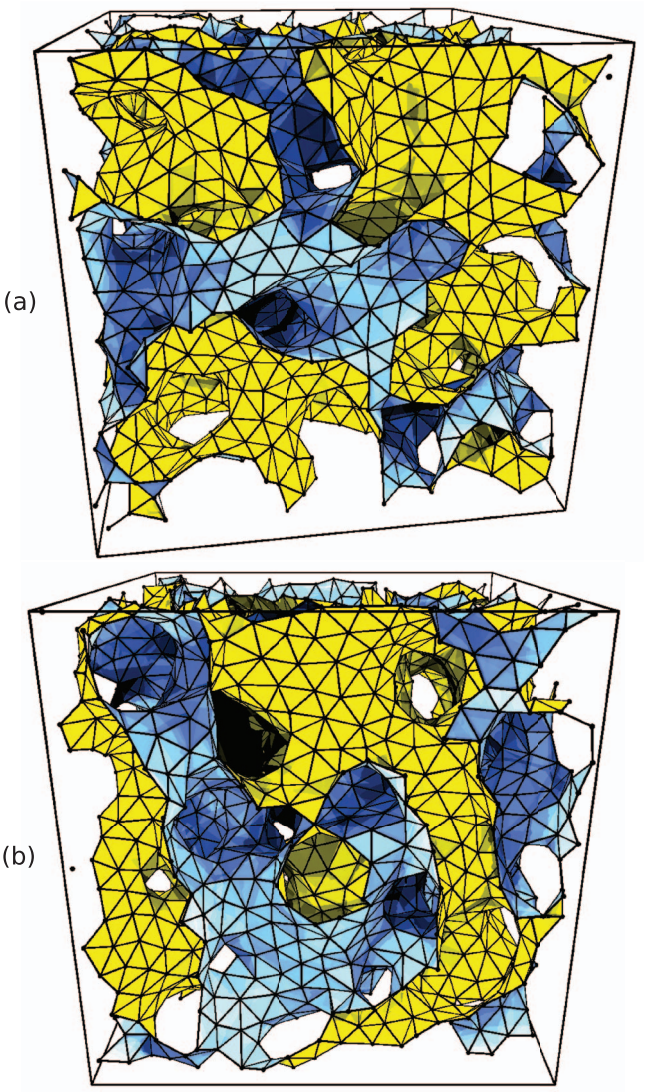

FIG. 2. Typical configurations from simulations for $N = 2207$ beads for $\kappa = 3.5$, $\bar{\kappa} = -0.6$, and $p = 0.01$ (upper panel) as well as for $\kappa = 5.0$, $\bar{\kappa} = -0.6$, and $p = 0.03$ (lower panel). The two sides of the membrane are colored differently to make the bicontinuous structure more easily visible. A view of the structure for $\kappa = 3.5$, $\bar{\kappa} = -0.6$, and $p = 0.01$ from different angles to reveal the shape and topology more clearly, and an animation of the temporal evolution of the microemulsion structure are shown (enhanced online) (a) [URL: http://dx.doi.org/10.1063/1.3701265.1], (b) [URL: http://dx.doi.org/10.1063/1.3701265.2].

fluctuate as a consequence of Euler's theorem. This implies that the number of attempted bond moves per Monte Carlo step must now be adjusted in such a way that the probability for a bond-flip attempt is constant, independent of the topology. This can easily be done by relating the number of bond flips to the actual total number of bonds of each configuration.

Examples of the microemulsion configurations generated by this simulation are plotted in Fig. 2 for two values of the bending rigidity κ. The different membrane shapes indicate that the structure becomes more correlated for larger values of κ, as can be seen quantitatively from the correlation length discussed in Sec. IV B below.

The most important quantities describing the structure of the microemulsion that we calculate here are the scattering intensities in bulk and film contrast. These are used here in order to facilitate direct comparisons with experiments. The details on their calculation from the simulations are explained in the Appendix. All scattering intensities in film and bulk contrast are computed from the simulated configurations using Eqs. (A6) and (A8), respectively.

IV. RESULTS

A. Equation of state

We start by calculating the equation of state of the microemulsion in order to compare with earlier simulation results[43] and theoretical predictions. More specifically, we wish to determine the dependence of the surfactant density on the applied pressure. The expected behavior to the lowest order in the surfactant volume fraction ϕ is given by scaling arguments as[58]

$$p \propto \phi^3. \tag{32}$$

Two kinds of corrections have been discussed. On one hand, since the scaling argument leading to Eq. (32) assumes small volume fractions, the form $p = a\phi^3 + b\phi^5$ incorporating a next-to-leading order correction as ϕ^5 has been suggested.[59,60] On the other hand, the bending rigidity κ and the saddle-splay modulus $\bar{\kappa}$ are logarithmically renormalized by thermal fluctuations as discussed in Sec. II C. In contrast to the high-density correction, the renormalization becomes important at low densities, i.e., at high dilution, since the role of the length scale in the renormalization is played by the inverse area density $(S/V)^{-1}$ of the surfactant monolayer. Therefore, a logarithmic correction to the equation of state as $p = \phi^3[b_1 + b_2 \log \phi]$ has been proposed.[27] Note that these two corrections come into play in different regimes, and therefore observing either one in a given system does not rule out the possibility of the other. The low-density correction plays an important role in the derivation of the phase diagram of surfactant solutions by considering instabilities destroying the lamellar phase,[28–30] as discussed in Sec. II C above.

We plot the equation of state as measured from our simulations in Fig. 3. All data are shown for $N = 2207$ vertices. The plot clearly indicates that the equation of state is well described by the form

$$\frac{p\delta^3}{k_B T} = [A(\kappa, \bar{\kappa}) + B(\kappa, \bar{\kappa}) \ln(\phi)]\, \phi^3, \tag{33}$$

as proposed on the basis of membrane-elasticity renormalization. Here, we define the membrane volume fraction as $\phi = \delta S/V$, with an effective membrane thickness δ. For simplicity, we use $\delta = a_0$, i.e., we identify the membrane thickness with the diameter of the hard spheres at the membrane vertices; this is certainly an over-estimation of the effective membrane fraction. We will come back to this point in Sec. V.

The simulation data show that the coefficient $A(\kappa, \bar{\kappa})$ in Eq. (33) is essentially independent of κ and depends linearly on $\bar{\kappa}$, and that $B(\kappa, \bar{\kappa})$ is independent of both κ and $\bar{\kappa}$. A fit of the data shown in Fig. 3 with the linear dependence $A(\bar{\kappa}) = -(c + d\bar{\kappa})$, yields the values $c \approx 0.543$, $d \approx 2.77$, and $B \approx 0.964$. The corresponding fits are shown

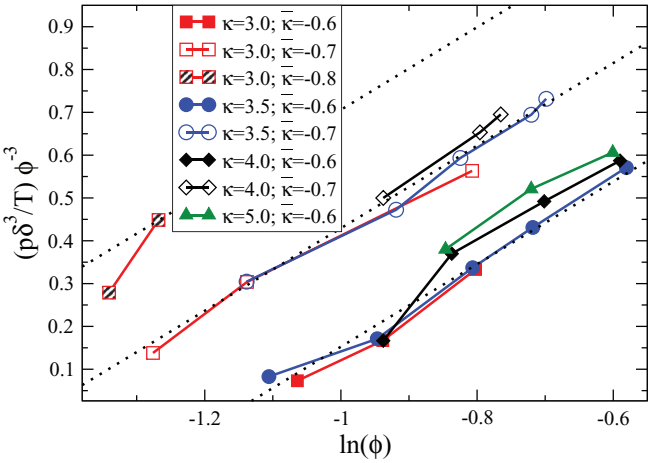

FIG. 3. The equation of state $[p(\phi)\delta^3/T]\phi^{-3}$ vs. $\ln(\phi)$ of sponge phases for several values of κ and $\bar{\kappa}$ as indicated by the legend. All data are for system size $N = 2207$. The symbols show the simulation results, and the thick dotted lines are the fits as discussed in the text.

in Fig. 3. These results confirm and strengthen earlier ones[43] concerning the same system but for considerably smaller values of κ (and smaller system sizes). The present results are more reliable, however, since larger values of κ lead to smoother surfaces and larger domain sizes, and consequently there are fewer discretization artifacts.

B. Bulk scattering

We now turn to the scattering intensity in bulk contrast. We calculate the bulk scattering intensity from the simulated configurations using Eq. (A8). Examples are depicted in Fig. 4(a) for varying bending rigidity κ and in Fig. 4(b) for varying pressure. In Fig. 4(a), the Teubner-Strey equation (5) has been fitted to all curves around the scattering peak. More precisely, we have used non-weighted least-squares fits in the region $q\delta \in (0, 2]$. The fit around the peak is good, but in the large-q tail the amplitudes of the power law decay are different in Eq. (5) and the simulation data. This difference is expected, however, because the considerations leading to Eq. (5) as discussed above concern the structure of the microemulsion at length scales around the structural length scale of the system, whereas the scattering intensity at large q is determined by the local interface structure at small scales. In our case, these interfaces are locally flat, and the corresponding scattering properties are given by the Porod laws discussed above in Sec. II E.

In order to check the Porod law for bulk scattering, Eq. (20), we have fitted the large-q tail of $S_b(q)$ with a power law. In all cases, the exponent is -4. The amplitude is plotted in Fig. 5 as a function of S/V. Regardless of the values of κ and $\bar{\kappa}$, all data fall on a single straight line. This corresponds to our expectations. The roughness of the surface Σ in Eq. (20) vanishes, since for the largest q for which the term $\exp(-q^2\Sigma^2)$ in Eq. (20) becomes relevant the surface is made of flat triangles for which there is no roughness. A linear fit to the data in Fig. 5 yields the slope $a_b V/S \approx 5.86$, which is in reasonable agreement with the Porod result $a_b V/S = 2\pi$

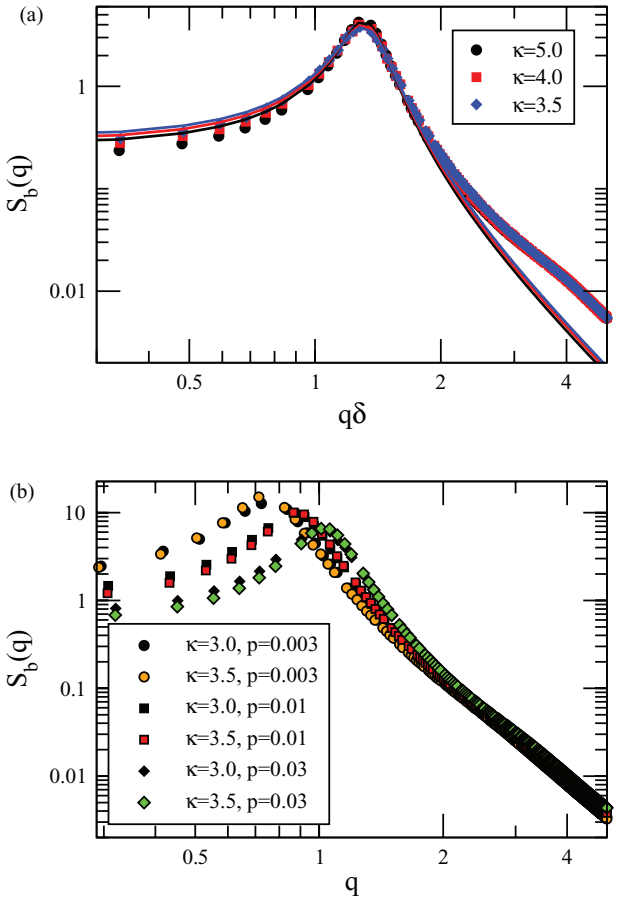

FIG. 4. Bulk scattering intensity $S_b(q)$ (symbols) as a function of the wave vector q for $p = 0.1$, $\bar{\kappa} = -0.6$, $N = 2207$, and several values of the bending rigidity κ (upper panel), and for $\bar{\kappa} = -0.6$, $N = 2207$, and several values of the bending rigidity κ and the osmotic pressure p (lower panel). In the upper panel, the solid lines are fits corresponding to the Teubner-Strey formula, Eq. (5), with the line colors matching the symbol colors in the corresponding simulation data.

(compare Eq. (20) with $\Delta\rho = 1$). In conclusion, the Porod low for bulk scattering is reproduced by our simulations.

Next, we analyze the microemulsion structure at length scales of the order of the structural length scale $(S/V)^{-1}$. Each data set is fitted to the Teubner-Strey equation (5) and the coefficients a, b, and c are extracted. Equation (7) is then used to compute the domain size $d = 2\pi/k_0$ and the correlation length ξ.

First, the domain size d, scaled by the structural length scale $(S/V)^{-1}$, is plotted as a function of S/V for several values of κ and $\bar{\kappa}$ in Fig. 6 for two system sizes. For $N_p = 2207$, there is a weak dependence on S/V for small S/V and $\kappa \leq 3.5$; otherwise dS/V is independent S/V. Likewise, for $N_p = 607$ the dependence of dS/V on S/V is also either weak or absent, which implies that finite-size effects are small. For both cases, the prediction by GRFM follows from Eq. (12) and is a constant $dS/V = 4/\sqrt{3} \approx 2.3094$. Comparison with Fig. 6 shows that this agrees almost quantitatively with a deviation of only about 15%.

Second, the correlation length $\xi S/V$ is plotted in Fig. 7 as a function of S/V for system sizes $N = 2207$ (main figure) and $N = 607$ (inset). Now, in contrast to the scaled domain size, dS/V, a dependence on all three parameters, S/V, κ, and

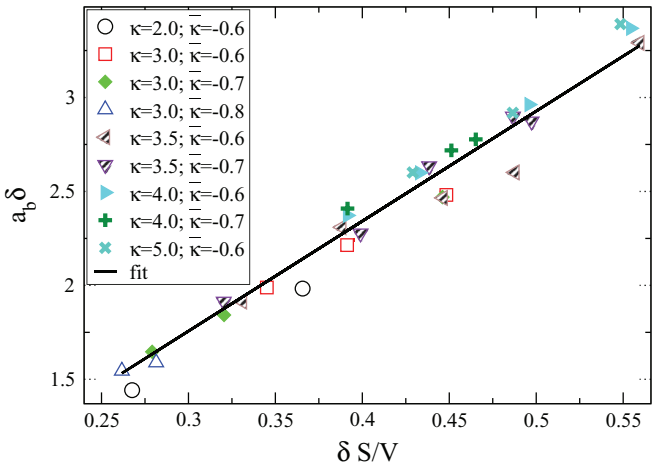

FIG. 5. The amplitude of the large-q tail of the bulk scattering intensity $S_b(q)$ as a function of S/V for several values of κ and $\bar{\kappa}$, together with a linear fit forced to go through the origin.

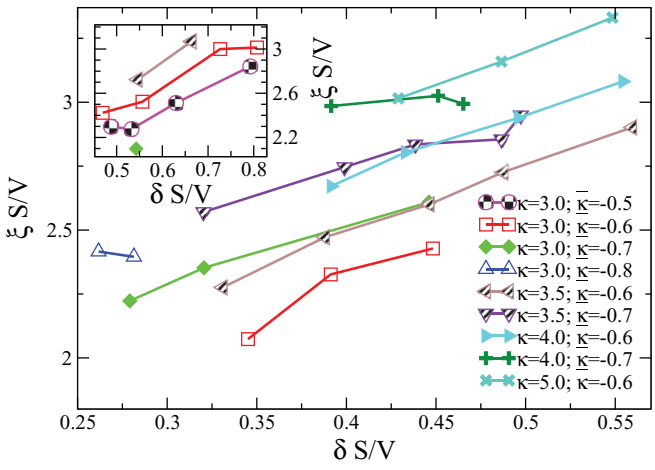

FIG. 7. The correlation length $\xi S/V$ as a function of S/V for several values of κ and $\bar{\kappa}$ for system size $N = 2207$. The inset shows the same for $N = 607$.

$\bar{\kappa}$ is found. This should be compared to the prediction given by GRFM, Eq. (13), where $\xi S/V \propto \kappa$ and no dependence on $\bar{\kappa}$ or the density S/V is expected. The predicted values are $\xi S/V \approx 8.15$, 9.51, 10.87, and 13.58 for $\kappa = 3.0$, 3.5, 4.0, and 5.0, respectively, approximately a factor of 4 larger than the simulation data. The simulation results for the correlation length are qualitatively different than the predictions of the GRFM.

Finally, let us look at the length scale ratio $k_0\xi$. As a dimensionless number describing the structure of the microemulsions, this forms our main observable, for which comparisons to experiments are also easily possible. The length scale ratio $k_0\xi$ is plotted in Fig. 8 for $N = 2207$ and $N = 607$. Like the correlation length, $\xi S/V$, $k_0\xi$ depends on κ, $\bar{\kappa}$, and S/V. Most importantly, due to the $\bar{\kappa}$-dependence, it differs qualitatively from the predictions of GRFM.

Based on the simulation data shown in Fig. 8(a), we propose that $k_0\xi$ can be described as a linear combination of the renormalized bending rigidity κ_R and the renormalized saddle-splay modulus $\bar{\kappa}_R$ as

$$k_0\xi = \frac{64}{5\sqrt{3}}\left[a\kappa_R(l) + \bar{a}\bar{\kappa}_R(l)\right], \tag{34}$$

where a and $\bar{a}$ are dimensionless coefficients, which we determine below. The values $a = 1$ and $\bar{a} = 0$ correspond to the predictions of the augmented GRFM. Plugging the renormalized material parameters in Eqs. (15) and (16) into

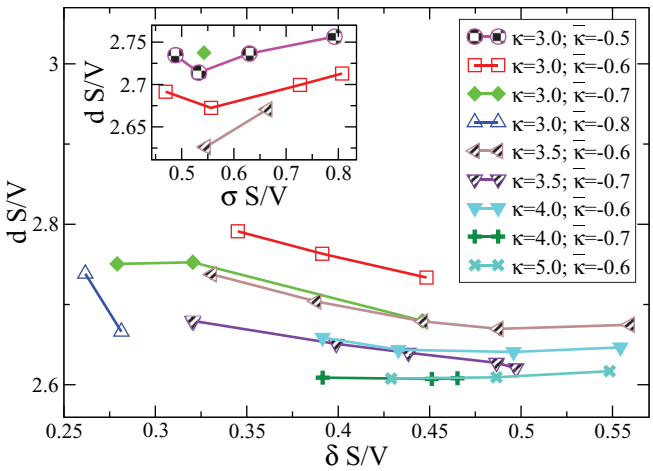

FIG. 6. The scaled domain size, dS/V, as a function of S/V for several values of κ and $\bar{\kappa}$ for system size $N = 2207$. The inset shows the same for $N = 607$.

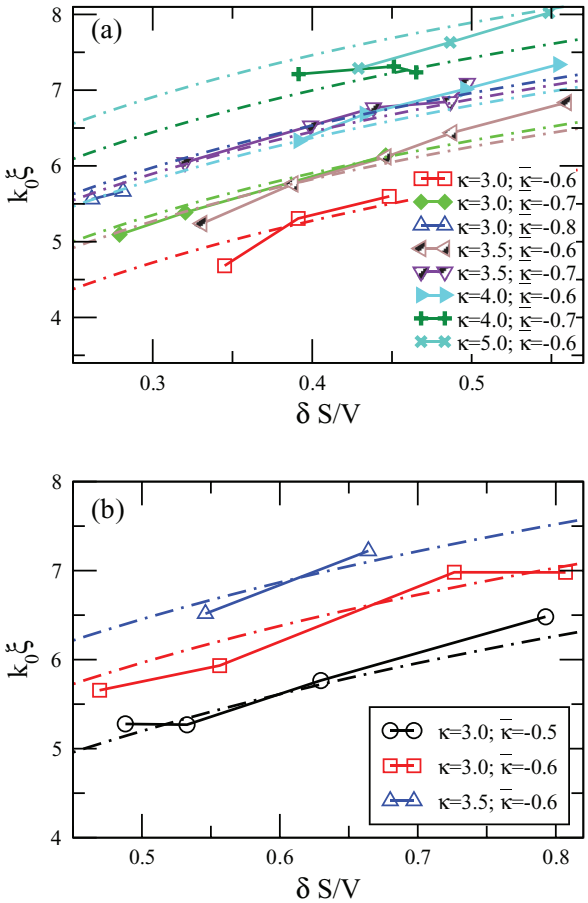

FIG. 8. The length scale ratio $k_0\xi$ as a function of S/V for several values of κ and $\bar{\kappa}$ for system sizes (a) $N = 2207$ and (b) $N = 607$. The symbols show the simulation results and the dashed-dotted lines are the fits discussed in the text. The color coding indicates which values of κ and $\bar{\kappa}$ the dashed-dotted lines correspond to.

Eq. (34) yields

$$k_0\xi = \frac{64}{5\sqrt{3}}\left\{(a\kappa + \bar{a}\bar{\kappa}) + (a\alpha + \bar{a}\bar{\alpha})\,\frac{1}{4\pi}\ln\left(\delta\frac{S}{V}\right)\right\}. \tag{35}$$

Here, the thickness δ of the surfactant layer is taken to be the same as the bead diameter a_0 of the triangulated-surface model. We have fitted Eq. (35) to the complete data set shown in Fig. 8(a). The resulting values for the coefficients are

$$a \approx 0.148 \quad \text{and} \quad \bar{a} \approx -0.849\,,$$

so that

$$k_0\xi = \frac{64}{5\sqrt{3}}\left\{(0.15\kappa - 0.85\bar{\kappa}) + \frac{3.27}{4\pi}\ln\left(\delta\frac{S}{V}\right)\right\}. \tag{36}$$

This shows that the dependence of $k_0\xi$ on $\bar{\kappa}$ is more pronounced than on κ. Equation (36) is plotted in Fig. 8(a) as a function of S/V separately for all values of κ and $\bar{\kappa}$. We observe a reasonable agreement. Note that the fitting procedure itself has been applied simultaneously on all of the data, i.e., for all simulated values of p, κ, and $\bar{\kappa}$.

A similar analysis for the smaller system size with $N_p = 607$ has also been performed. The results are shown in Fig. 8(b). The resulting coefficients are $a \approx 0.132$ and $\bar{a} \approx -1.038$. These differ slightly for those reported for $N_p = 2207$ above. Since the differences are small, we believe that the results for the larger system are more reliable and essentially unaffected by finite-size effects.

The fact that Eq. (34) describes the simulation data better than the augmented GRFM is one of our main results. We wish to emphasize, however, that the exact form of Eq. (34) — the simple linear combination of renormalized κ and $\bar{\kappa}$ — is for the moment not supported by any rigorous theoretical arguments. Instead, it is the simplest possible ansatz we can make that describes the simulation data well. No theories for $k_0\xi$ with a resulting $\bar{\kappa}$ dependence exist. The current results underline the need for developing the theory of microemulsions further.

C. Film scattering

Examples of the scattering intensity in film contrast are shown in Fig. 9. Compared to the bulk scattering intensities discussed above, the scattering peak is less pronounced, as is well known from experiment. The tail is well fitted with a power law $S_f(q) \sim q^{-2}$ for large q as predicted by the Porod law, Eq. (21).

In order to check the Porod law for simulated film scattering more precisely, we have fitted the large-q tail of the film scattering intensity $S_f(q)$ with a power law decay. The exponent is invariably -2. As was the case with the bulk scattering intensity, the simulated surfactant layers are not rough. Therefore, the surface roughness $\Sigma = 0$ in Eq. (21). The amplitude of the q^{-2} decay is determined by the fits to the simulation data, and is plotted in Fig. 10 as a function of S/V. The dependence is linear as expected, and a fit reveals the slope $a_f V/S \approx 6.173$, which is reasonably close to the predicted value $a_f V/S = 2\pi$ (compare Eq. (21) with $\Delta\rho = 1$). As a

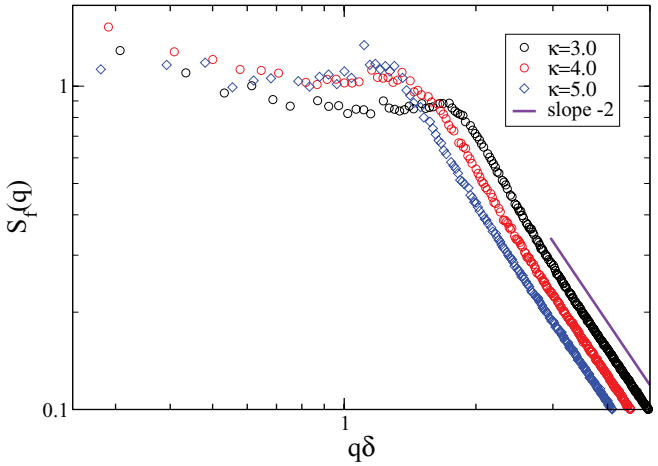

FIG. 9. Film scattering intensity $S_f(q)$ as a function of the wave vector q for $p = 0.01$, $\bar{\kappa} = -0.6$, $N_p = 2207$, and several values of the bending rigidity κ together with a power law fit to the tail (line shifted upwards for clarity).

conclusion, the simulation reproduces also the Porod law for scattering in film contrast.

We focus now on the film scattering intensity in the region $q < 2k_0$. Figure 11 shows cases with a clear peak in the scattering intensity (at higher surfactant density) together with ones having a mere shoulder (at lower surfactant density). In all cases we have simulated, the peak or shoulder in the film scattering is located at $q = 2k_0$ (with k_0 being the peak position in the bulk scattering for the same set of parameters). This is completely in line with the theoretical predictions,[36,51] and also indicates that simulation results for film and bulk scattering are mutually compatible. Comparisons between least-squares fits to Eq. (19) and simulation data are shown in Fig. 11, where α and β play the role of the fitting parameters. In all cases, the predicted dependence is recovered in the low-q region, although the data are somewhat noisy. This region is not visible in all data sets however, since, depending on the value of k_0 for a given data set, the region $q < 2k_0$ can become prohibitively narrow. Considering the values for the data sets depicted in Fig. 11, we find that α is independent of

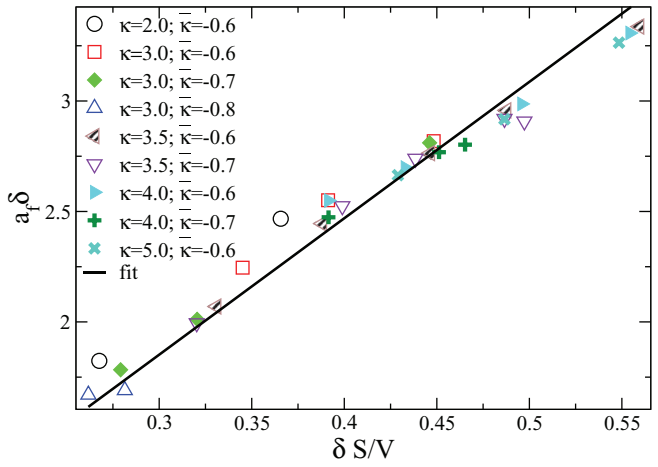

FIG. 10. The amplitude a_f of the large-q tail of the film scattering intensity $S_f(q)$ as a function of S/V for several values of κ an $\bar{\kappa}$, together with a linear fit forced to go through the origin.

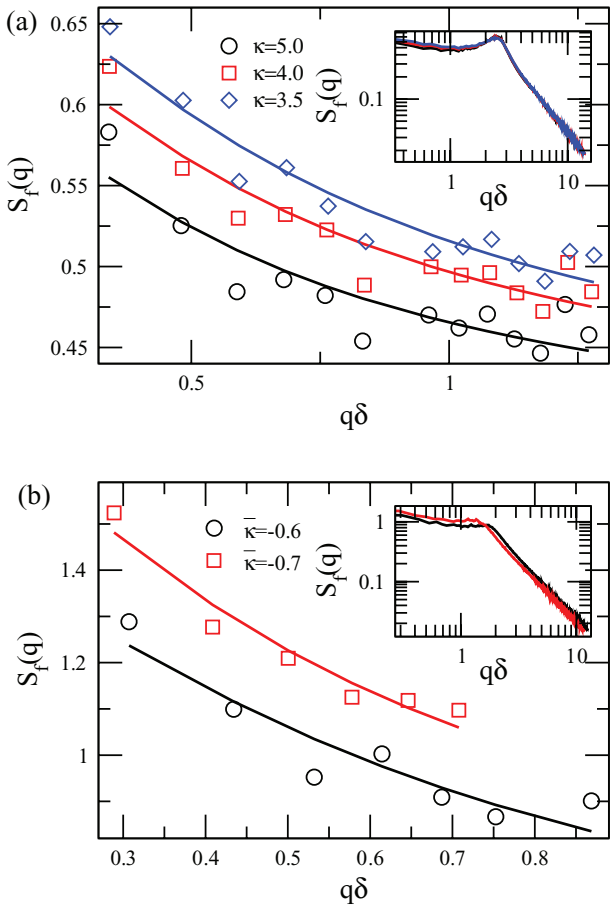

FIG. 11. The small-q behavior of the film scattering intensity for various cases. (a) $\bar{\kappa} = -0.6$, $p = 0.1$, $N = 2207$, and κ varies as indicated by the legend. (b) $\kappa = 3.0$, $p = 0.01$, $N = 2207$, and $\bar{\kappa}$ varies as indicated by the legend. The main panels show the small-q part of $S_f(q)$ on linear scale, where the full lines are fits to Eq. (19). The insets display the full scattering functions on double-logarithmic scales. The colors of the data sets in the insets match those in the main figures.

κ and an increasing function of $|\bar{\kappa}|$, whereas β is a decreasing function of both κ and $|\bar{\kappa}|$.

D. Topology

Finally, we study the topology of the sponge phases using the scaled Euler characteristic[43,45]

$$\gamma = \langle \chi_E V^2 S^{-3} \rangle, \tag{37}$$

where χ_E is the Euler characteristic defined in Eq. (26), V is the volume of the system, and S is the total area of the membrane. The scaled Euler characteristic γ is used instead of χ_E, since as an extensive quantity χ_E is not a good measure of the connectivity of a sponge phase. We plot γ as a function of the surfactant density $\delta S/V$ in Fig. 12 for several values of κ and $\bar{\kappa}$.

The simulation data strongly suggest that γ depends logarithmically on $\delta S/V$,

$$\gamma = \gamma_0(\kappa, \bar{\kappa}) + \gamma_1 \ln\left(\delta \frac{S}{V}\right), \tag{38}$$

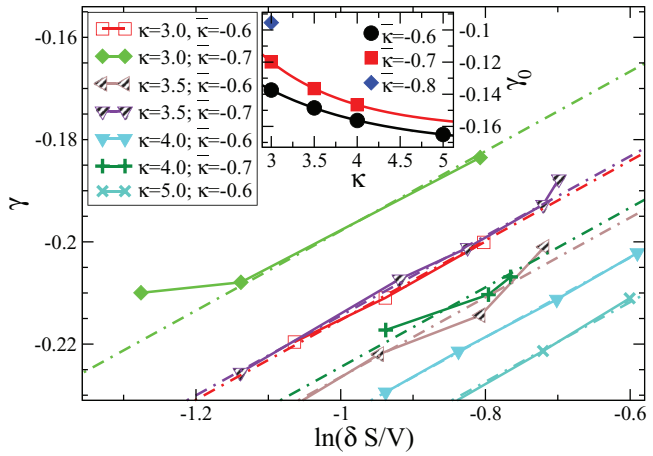

FIG. 12. The scaled Euler characteristic $\gamma = \langle \chi_E V^2 S^{-3} \rangle$, as a function of the surfactant density $\delta S/V$. The symbols denote the simulation data for various values of κ and $\bar{\kappa}$, as indicated. The dashed-dotted lines are a least-squares fit to Eq. (38). The inset shows the constant term γ_0 in Eq. (38) as a function of κ for different values of $\bar{\kappa}$. The solid lines are guides to the eye.

where the prefactor of the logarithmic term γ_1 does not appear to depend on κ or $\bar{\kappa}$, whereas the constant term γ_0 is a function of both κ and $\bar{\kappa}$. We have performed a least-squares fit to Eq. (38). The results indicate that $\gamma_1 \approx 0.078$. The dependence of the constant term γ_0 on κ and $\bar{\kappa}$ is plotted in Fig. 12. Here, γ_0 is found to be a decreasing function of κ and an increasing function of $\bar{\kappa}$. Note that GRFM predicts an universal constant $\gamma_{GRF} = -\pi/16 \approx -0.196$ for all interaction kernels $V(\vec{q})$, see Eq. (8).[33] The GRFM prediction falls well within the range of the simulation results, but lacks the systematic dependencies of γ on κ, $\bar{\kappa}$, and S/V noted above. It is also interesting to note that the topology of the ordered gyroid (G) phase is characterized by $\gamma_G = -0.271$.[61] With increasing κ, the γ values in Fig. 12 indeed become more negative, consistent with the structure becoming more like a minimal surface.

V. DISCUSSION AND CONCLUSIONS

We have studied the scattering intensities in bulk and film contrast of bicontinuous microemulsions using Monte Carlo simulations of a dynamically triangulated surface. The topology of the surface is allowed to fluctuate.[43]

The bulk scattering intensity of microemulsions shows a peak with a position and width, or equivalently, two length scales, the domain size and the correlation length. We characterize the dependence of the dimensionless ratio $k_0\xi$ of these two length scales as a function of the bending rigidity, the saddle-splay modulus, and the surfactant density, which is coupled to the applied osmotic pressure by the equation of state. An existing theory, the GRFM,[35,36] predicts that $k_0\xi$ should depend linearly on κ and be independent of $\bar{\kappa}$. On the other hand, κ and $\bar{\kappa}$ have been shown to depend logarithmically on the investigated length scale, and thus on the surfactant density.[37]

Here, we have demonstrated by simulations that $k_0\xi$ depends on all three parameters, κ, $\bar{\kappa}$, and density S/V. Furthermore, the dependence on $\bar{\kappa}$ is stronger than that on κ. This

differs qualitatively from the GRFM predictions. In order to characterize the discrepancy further, we have fitted a simple ansatz, Eq. (36), which is a linear combination of the renormalized κ and $\bar{\kappa}$ with universal prefactors, to the simulation data. The analysis clearly indicates that this form of the dependence describes the simulation data better than the earlier predictions.

It is important to point out that the new result (Eq. (36)) is not inconsistent with the previous analysis of scattering data in Ref. 16, which was based on the assumption of a linear dependence of $k_0\xi$ on κ_R only. The reason is that the prefactor of the logarithm in Eq. (36) is nearly the same — $3.27/(4\pi)$ versus $3/(4\pi)$ — so that the S/V-dependence is essentially identical in both cases, and the extraction of the bare elastic moduli of the membrane can proceed quantitatively in the same way. However, an analysis of $k_0\xi$ no longer gives direct access to the bare κ, as assumed in Ref. 16 but only to the linear combination $(0.15\kappa - 0.85\bar{\kappa})$.

The parameter δ plays a double role in the analysis of the simulation data. On the one hand, it is the cutoff in the fluctuation spectrum of a membrane; on the other hand, the effective membrane thickness needed to define a membrane volume fraction. We have identified both lengths with the hard-core diameter of the membrane beads. In a real membrane, these parameters will be of similar magnitude but have not to be identical. This raises the obvious question, how strongly our analysis and the conclusions are affected by the choice of δ. First, in the definition of the membrane volume fraction, the effective membrane thickness mainly appears as a length unit. The results in most of our figures can be easily transformed to any other choice of membrane thickness; for example, a choice $\delta = a_0/2$ would simply reduce the volume fractions in Figs. 6–8 by a factor 2. Second, our main result of the dependence of $k_0\xi$ on κ, $\bar{\kappa}$, and S/V does not depend on the membrane thickness. Here, δ only enters as a fluctuation cutoff. Since δ appears in the logarithm, a different choice of δ only adds an additive constant but does not affect the functional dependences. However, we want to emphasize that the values of κ and $\bar{\kappa}$ extracted from an experiment would be (mildly) affected by the definition of δ.

The main result of our analysis, Eq. (36), raises the question of the origin of the $\bar{\kappa}$-dependence. Figures 6 and 7 demonstrate that both length scales, domain size and correlation length, depend on $\bar{\kappa}$. The domain size d decreases and the correlation length ξ increases with increasing $\bar{\kappa}$. The former effect can be understood as the creation of passages, Fig. 1, becoming more favorable for increasing $\bar{\kappa}$ creating connections between parallel membranes. Such connections lead to entropic attraction between the membranes,[31,38] i.e., the passages tend to draw the membranes closer to each other. To understand the latter effect, we note that the membranes under consideration are almost minimal surfaces (of vanishing mean curvature) for all but the smallest values of the bending rigidity κ. The requirement of almost vanishing average curvature reduces the available configuration space rather strongly. The more connections between the surfaces are introduced for larger $\bar{\kappa}$, the more correlated are the membrane positions, since the average curvature remains pointwise small. This can be speculated to lead to larger correlation lengths ξ.

This is connected to the behavior of the scaled Euler characteristic, Eq. (37). While a constant value $\gamma = -\pi/16 \approx -0.196$ is predicted by the GRFM, the values for triply periodic minimal surfaces range from approximately -0.271 to -0.370 for different surfaces.[61] The values for the lowest studied κ and highest densities S/V roughly correspond to the GRFM prediction, but there is a consistent trend to higher values of $|\gamma|$ with growing κ and the description of the system as an approximative minimal surface becomes more appropriate. Furthermore, different minimal surfaces have a different Euler characteristic or, equivalently, a different number of passages per unit volume. Since the parameter $\bar{\kappa}$ directly controls the energetical favorability of the passages, the scaled Euler characteristic γ is expected to depend on $\bar{\kappa}$. Indeed, such a dependence is seen in the simulation results, see Fig. 12. Furthermore, $|\gamma|$, which is proportional to the number of handles per unit volume, decreases with an increasing $\bar{\kappa}$ as the connections become energetically less favorable. This trend is clearly seen in the simulation data.

In addition to characterizing $k_0\xi$, we have extracted the equation of state from the simulations, with $p = \phi^3[b_1 + b_2 \log \phi]$. Thus, the dominating correction to the first order scaling $p \propto \phi^3$ is logarithmic, following from the logarithmic rescaling of bending rigidity and saddle-splay modulus. We have also demonstrated that the simulations reproduce the Porod laws for bulk[12,52] and film[53] scattering qualitatively. Finally, we have shown that the low-q behavior of the scattering intensity in film scattering matches theoretical predictions of a q^{-1} behavior.

This study opens up many directions for future work. On the theoretical side, a theory of the microemulsion structure that can explain the dependence of the scattering intensity on $\bar{\kappa}$ is required. On the experimental side, our results show a new possibility for measuring the – often elusive – saddle-splay modulus.

ACKNOWLEDGMENTS

Discussions with T. Auth, H. Frielinghaus, O. Holderer, M. Monkenbusch, and D. Richter are gratefully acknowledged.

APPENDIX: SCATTERING INTENSITIES OF TRIANGULATED SURFACES

Consider first the film scattering intensity at wave vector $\vec{q}$ from a triangle A whose corners are given by the position vectors $\vec{r}_1$, $\vec{r}_2$, and $\vec{r}_3$. The film scattering amplitude from this triangle is then given by the integral

$$I_f(q;\vec{r}_1,\vec{r}_2,\vec{r}_3) = \int_A \mathrm{d}^2 r e^{i\vec{q}\cdot\vec{r}}. \tag{A1}$$

In order to evaluate Eq. (A1), parametrize the surface of the triangle through t_1 and t_2 as

$$\vec{r} = \vec{r}_1 + t_1(\vec{r}_2 - \vec{r}_1) + t_2(\vec{r}_3 - \vec{r}_1) \tag{A2}$$

so that Eq. (A1) can be written as an integral over t_1 and t_2 as

$$I_f = \int_0^1 \mathrm{d}t_1 \int_0^{1-t_1} \mathrm{d}t_2 \sqrt{\det \rho}\, e^{iq\cdot[\vec{r}_1 + t_1(\vec{r}_2-\vec{r}_1)+t_2(\vec{r}_3-\vec{r}_1)]}, \tag{A3}$$

where

$$\sqrt{\det \rho} = (\vec{r}_2 - \vec{r}_1) \times (\vec{r}_3 - \vec{r}_1). \tag{A4}$$

Equation (A3) can be evaluated to

$$I_f(q;\vec{r}_1,\vec{r}_2,\vec{r}_3) = \sqrt{\det \rho}\left[\frac{\exp(i\vec{q}\cdot\vec{r}_1)}{\vec{q}\cdot(\vec{r}_1-\vec{r}_3)\vec{q}\cdot(\vec{r}_2-\vec{r}_1)} + \frac{\exp(i\vec{q}\cdot\vec{r}_2)}{\vec{q}\cdot(\vec{r}_2-\vec{r}_1)\vec{q}\cdot(\vec{r}_3-\vec{r}_2)} + \frac{\exp(i\vec{q}\cdot\vec{r}_3)}{\vec{q}\cdot(\vec{r}_3-\vec{r}_1)\vec{q}\cdot(\vec{r}_2-\vec{r}_3)}\right]. \tag{A5}$$

The film scattering intensity of the microemulsion is then the sum of Eq. (A5) over all triangles of the surface normalized by volume, i.e.,

$$S_f(q) = \frac{1}{V}\left|\sum_{i=1}^{N_t} I_f(q;\vec{r}_1^{(i)},\vec{r}_2^{(i)},\vec{r}_3^{(i)})\right|^2. \tag{A6}$$

In contrast to the film scattering intensity, the bulk scattering intensity is evaluated as a three-dimensional volume integral instead of the surface integral of Eq. (A1). However, since the surface is closed due to the periodic boundary conditions, we can express it as a surface integral using the divergence theorem. This results in the scattering amplitude

$$I_b(q;\vec{r}_1,\vec{r}_2,\vec{r}_3) = -\frac{1}{q^2}(\hat{n}\cdot\vec{q})I_f(q;\vec{r}_1,\vec{r}_2,\vec{r}_3), \tag{A7}$$

where $I_f(q;\vec{r}_1,\vec{r}_2,\vec{r}_3)$ is given by Eq. (A1). Here, $\hat{n}$ is the outward-facing unit normal vector, and the fact that it is a constant within a triangle has been used. Note that in order to evaluate this expression, the surface has to be oriented. As above, the bulk scattering intensity of the microemulsion is computed as a sum over all triangles of the surface normalized by volume,

$$S_b(q) = \frac{1}{V}\left|\sum_{i=1}^{N_t} I_b(q;\vec{r}_1^{(i)},\vec{r}_2^{(i)},\vec{r}_3^{(i)})\right|^2. \tag{A8}$$

[1] *Micelles, Membranes, Microemulsions, and Monolayers*, edited by W. M. Gelbart, A. Ben-Shaul, and D. Roux (Springer-Verlag, Berlin, 1994).
[2] G. Gompper and M. Schick, in *Phase Transitions and Critical Phenomena*, edited by C. Domb and J. Lebowitz (Academic, London, 1994), Vol. 16, pp. 1–176.
[3] J. Schulman and J. Montagne, Ann. N.Y. Acad. Sci. **92**, 366 (1961).
[4] P. De Gennes and C. Taupin, J. Phys. Chem. **86**, 2294 (1982).
[5] G. Porte, J. Phys. Condens. Matter **4**, 8649 (1992).
[6] S. A. Safran, *Statistical Thermodynamics of Surfaces, Interfaces, and Membranes* (Addison-Wesley, Reading, MA, 1994).
[7] G. Gompper and D. Kroll, J. Phys. Condens. Matter **9**, 8795 (1997).
[8] U. Seifert, Adv. Phys. **46**, 13 (1997).
[9] *Statistical Mechanics of Membranes and Surfaces*, edited by D. Nelson, T. Piran, and S. Weinberg (World Scientific, Singapore, 2004).
[10] G. Porte, M. Delsanti, I. Billard, M. Skouri, J. Appell, J. Marignan, and F. Debeauvais, J. Phys. II (France) **1**, 1101 (1991).
[11] M. Teubner and R. Strey, J. Chem. Phys. **87**, 3195 (1987).
[12] T. Sottmann, R. Strey, and S. Chen, J. Chem. Phys. **106**, 6483 (1997).
[13] T. Sottmann and R. Strey, J. Chem. Phys. **106**, 8606 (1997).
[14] H. Endo, J. Allgaier, G. Gompper, B. Jakobs, M. Monkenbusch, D. Richter, T. Sottmann, and R. Strey, Phys. Rev. Lett. **85**, 102 (2000).
[15] H. Endo, M. Mihailescu, M. Monkenbusch, J. Allgaier, G. Gompper, D. Richter, B. Jakobs, T. Sottmann, R. Strey, and I. Grillo, J. Chem. Phys. **115**, 580 (2001).
[16] G. Gompper, H. Endo, M. Mihailescu, J. Allgaier, M. Monkenbusch, D. Richter, B. Jakobs, T. Sottmann, and R. Strey, Europhys. Lett. **56**, 683 (2001).
[17] T. Foster, T. Sottmann, R. Schweins, and R. Strey, J. Chem. Phys. **128**, 064902 (2008).
[18] O. Holderer, H. Frielinghaus, D. Byelov, M. Monkenbusch, J. Allgaier, and D. Richter, J. Chem. Phys. **122**, 094908 (2005).
[19] M. Monkenbusch, O. Holderer, H. Frielinghaus, D. Byelov, J. Allgaier, and D. Richter, J. Phys. Condens. Matter **17**, S2903 (2005).
[20] O. Holderer, M. Klostermann, M. Monkenbusch, R. Schweins, P. Lindner, R. Strey, D. Richter, and T. Sottmann, Phys. Chem. Chem. Phys. **13**, 3022 (2011).
[21] M. Klostermann, T. Foster, R. Schweins, P. Lindner, O. Glatter, R. Strey, and T. Sottmann, Phys. Chem. Chem. Phys. **13**, 20289 (2011).
[22] B. Farago, M. Monkenbusch, K. Goecking, D. Richter, and J. Huang, Physica B: Condens. Matter **213**, 712 (1995).
[23] O. Holderer, H. Frielinghaus, M. Monkenbusch, J. Allgaier, D. Richter, and B. Farago, Eur. Phys. J. E **22**, 157 (2007).
[24] M. Mihailescu, M. Monkenbusch, H. Endo, J. Allgaier, G. Gompper, J. Stellbrink, D. Richter, B. Jakobs, T. Sottmann, and B. Farago, J. Chem. Phys. **115**, 9563 (2001).
[25] I. Barnes, S. Hyde, B. Ninham, P. Derian, M. Drifford, and T. Zemb, J. Phys. Chem. **92**, 2286 (1988).
[26] L. Liu, P. Bauduin, T. Zemb, J. Eastoe, and J. Hao, Langmuir **25**, 2055 (2009).
[27] D. Andelman, M. Cates, D. Roux, and S. Safran, J. Chem. Phys. **87**, 7229 (1987).
[28] L. Golubovic and T. Lubensky, Europhys. Lett. **10**, 513 (1989).
[29] L. Golubovic and T. Lubensky, Phys. Rev. A **41**, 4343 (1990).
[30] D. Morse, Phys. Rev. E **50**, 2423 (1994).
[31] L. Golubović, Phys. Rev. E **50**, 2419 (1994).
[32] G. Gompper and M. Schick, Phys. Rev. B **41**, 9148 (1990).
[33] M. Teubner, Europhys. Lett. **14**, 403 (1991).
[34] M. Teubner, J. Chem. Phys. **92**, 4501 (1990).
[35] P. Pieruschka and S. Safran, Europhys. Lett. **22**, 625 (1993).
[36] P. Pieruschka and S. Safran, Europhys. Lett. **31**, 207 (1995).
[37] L. Peliti and S. Leibler, Phys. Rev. Lett. **54**, 1690 (1985).
[38] G. Gompper and J. Goos, Phys. Rev. E **50**, 1325 (1994).
[39] P. Pieruschka, S. Safran, and S. Marcelja, Phys. Rev. E **52**, 1245 (1995).
[40] G. Gompper and J. Goos, Phys. Rev. E **52**, 1248 (1995).
[41] G. Gompper and D. Kroll, J. Phys. I (France) **6**, 1305 (1996).
[42] G. Gompper and D. Kroll, in *Statistical Mechanics of Membranes and Surfaces*, edited by D. Nelson, T. Piram, and S. Weinberg (World Scientific, Singapore, 2004).
[43] G. Gompper and D. Kroll, Phys. Rev. Lett. **81**, 2284 (1998).
[44] G. Gompper and M. Schick, Phys. Rev. Lett. **65**, 1116 (1990).
[45] G. Gompper and M. Kraus, Phys. Rev. E **47**, 4301 (1993).
[46] W. Helfrich, Z. Naturforsch. **28**, 693 (1973).
[47] W. Helfrich, J. Phys. (France) **46**, 1263 (1985).
[48] F. David, in *Statistical Mechanics of Membranes and Surfaces*, edited by D. Nelson, T. Piram, and S. Weinberg (World Scientific, Singapore, 1989).
[49] W. Cai, T. Lubensky, P. Nelson, and T. Powers, J. Phys. II (France) **4**, 931 (1994).
[50] D. Roux, M. Cates, U. Olsson, R. Ball, F. Nallet, and A. Bellocq, Europhys. Lett. **11**, 229 (1990).
[51] G. Gompper and M. Schick, Phys. Rev. E **49**, 1478 (1994).
[52] S. Ciccariello, J. Goodisman, and H. Brumberger, J. Appl. Crystallogr. **21**, 117 (1988).
[53] R. Strey, J. Winkler, and L. Magid, J. Phys. Chem. **95**, 7502 (1991).
[54] G. Gompper and D. M. Kroll, Curr. Opin. Colloid Interface Sci. **2**, 373 (1997).
[55] C. Itzykson, in *Proceedings of the GIFT Seminar, Jaca 85*, edited by J. Abad *et al.* (World Scientific, Singapore, 1986), pp. 130–188.
[56] H. Noguchi and G. Gompper, Phys. Rev. E **72**, 011901 (2005).

[57]M. Allen and D. Tildesley, *Computer Simulation of Liquids* (Clarendon, Oxford, 1999).
[58]G. Porte, J. Appell, P. Bassereau, and J. Marignan, J. Phys. (France) **50**, 1335 (1989).
[59]H. Wennerström and U. Olsson, Langmuir **9**, 365 (1993).
[60]J. Daicic, U. Olsson, H. Wennerström, G. Jerke, and P. Schurtenberger, J. Phys. II (France) **5**, 199 (1995).
[61]U. Schwarz and G. Gompper, *Morphology of Condensed Matter*, Lecture Notes in Physics, Vol. 600, edited by K. Mecke and D. Stoyan (Springer-Verlag, Berlin, 2002), pp. 107–151.